Research Article

Atomic modulation and phase engineering of MoS$_2$ for boosting N$_2$ reduction

Yansong Jia[1,2,#], Guining Shao[1,2,#], Yang Li[1,2], Ruizhe Yang[3], Ming Huang[3] , Hua Huang[4], Min Liu[5], Gai Huang[4], Qunjie Lu[4], Chaohua Gu[1,2]

[1]Institute of Process Equipment, College of Energy Engineering, Zhejiang University, Hangzhou 310000, Zhejiang, China.
[2]Hydrogen Energy Institute, Zhejiang University, Hangzhou 310000, Zhejiang, China.
[3]Institute of Fundamental and Frontier Sciences, University of Electronic Science and Technology of China, Chengdu 611731, Sichuan, China.
[4]National Energy Key Laboratory For New Hydrogen-Ammonia Energy Technologies, Foshan Xianhu Laboratory, Foshan 528200, Guangdong, China.
[5]State Grid Zhejiang Electric Power CO., LTD Research Institute, Hangzhou 310000, Zhejiang, China.
[#]Authors contributed equally.

Correspondence to: Dr. Yang Li, College of Energy Engineering, Zhejiang University, No. 38, Zheda RD, Xihu District, Hangzhou 10000, Zhejiang, China. E-mail: ly21@zju.edu.cn; Dr. Ming Huang, Institute of Fundamental and Frontier Sciences, University of Electronic Science and Technology of China, No. 2006, Xiyuan Avenue, West Hi-Tech Zone, Chengdu 611731, Sichuan, China. E-mail: huangming@uestc.edu.cn

Abstract

Electrochemical nitrogen reduction reaction (ENRR) has emerged as a potential alternative to the conventional Haber-Bosch process for ammonia production. However, ENRR technology is still restricted by the limited Faradaic efficiency due to the hard-to-break N-N triple bond. Herein, inspired by the biomimetic catalyst, we developed a Fe-modulated MoS$_2$ catalyst (named Fe@MoS$_2$) as an efficient ENRR catalyst. Raman spectra, coupled with the X-ray absorption spectroscopy, demonstrate the introduction of Fe into the MoS$_2$ lattice and achieve partial 2H to 1T phase conversion. The presence of S-vacancies on MoS$_2$ substrates was observed on scanning transmission electron microscopy images. Operando infrared absorption spectroscopy confirms that the constructed catalytic site significantly reduces barriers to nitrogen activation. The synthesized Fe@MoS$_2$, with its superior geometric and electronic structures, exhibits a remarkable Faradaic efficiency of 19.7 ± 5.5% at -0.2 V *vs.* Reversible Hydrogen Electrode and a high yield rate of 20.2 ± 5.3 μg h^{-1} mg^{-1} at -0.8 V *vs.* Reversible Hydrogen Electrode. Therefore, this work provides a fresh direction for designing novel catalysts, eventually boosting the nitrogen reduction reaction

kinetics and accelerating the ENRR application.

Keywords: Nitrogen reduction, heteroatom doping, molybdenum disulfide, phase engineering

INTRODUCTION

Ammonia (NH_3) ranks among the most demanded chemical products in the world, playing an essential role in producing fertilizers, plastics, and medicines[1,2]. Furthermore, it is also an important carbon-free energy carrier, benefiting from its high hydrogen content (17.6 wt%) and high gravimetric energy density (3 kWh kg^{-1})[3,4]. The lower liquefaction difficulty makes it more convenient for storage and transportation[5]. Nowadays, the artificial synthesis of NH_3 heavily depends on the Haber-Bosch (H-B) method. The N_2 and H_2 are transformed into NH_3 on the catalyst surface under severe reaction conditions (400-600 °C, ~60 bar)[6-8]. However, the H-B process is energy-intensive and has high carbon emissions and high cost of raw materials (H_2)[9,10]. Therefore, it is necessary to search for a green NH_3 synthesis technology. Recently, an electrochemical nitrogen reduction reaction (ENRR) technology has been developed and can realize the N_2 to NH_3 conversion at ambient temperature, with H_2O as the hydrogen source[11,12]. The total cost and carbon footprint of NH_3 synthesis will be effectively reduced by driving ENRR using renewable energy sources[13]. Moreover, the simple process equipment makes flexible and decentralized NH_3 preparation possible. Nevertheless, the ENRR process is still restricted by low yield rates and Faradaic efficiency (FE). Thus, the pursuit of highly efficient electrocatalysts for ENRR is greatly desirable but challenging.

Mo-based nitrogenase enables N_2 fixation under ambient conditions[14,15], which inspired researchers to investigate biomimetic catalysts with similar elemental compositions. MoS_2, as a layered two-dimensional (2D) semiconductor material, possesses a large surface area and crystal phase[16-19]. Multi-variable interlayer stacking forms and tunable electronic structure make it a promising candidate in the field of electrocatalytic synthesis of NH_3[20-22]. Due to the difficulty of activating the non-polar N-N triple bond and the high adsorption barrier of N_2, the NH_3 yield rate and energy transfer efficiency in ENRR are limited. Moreover, the hydrogen evolution reaction (HER) has a close reaction equilibrium potential to that of ENRR, affecting the selectivity of ENRR in the aqueous phase and leading to unsatisfactory FE[23-25]. Therefore, several strategies have been reported to optimize the MoS_2-based catalysts for improving ENRR performance, including vacancy engineering[26,27], heteroatom doping[28,29], phase engineering[30,31], *etc.*

The catalytic activity and stability of MoS_2 with different phases vary greatly in ENRR. Lin *et al.*[30] compared the ENRR performance of the metastable phase (1T'- and 1T'''-MoS_2) and the stable phase (2H-MoS_2). Thanks to the high localized electron density around Mo-Mo, the NH_3 yield and FE of 1T'''- MoS_2 are approximately nine and 12 times higher than those of 2H-MoS_2, respectively. Besides, constructing defects on the MoS_2 basal plane can expose more active sites for N_2 adsorption. You *et al.*[32] successfully introduced S vacancies in natural molybdenite through a one-step annealing method. The electron structure at the Mo edge was altered, which optimized the free energy barrier of the rate-limiting step. The prepared rich S-vacancy MoS_2 exhibited significantly improved ENRR performance compared to the raw material. In addition, benefiting from the synergistic effect among different elements, superior ENRR activity can be achieved by doping heteroatoms in MoS_2. Zhao *et al.* synthesized Fe-doped MoS_2 nanosheets (Fe-MoS_2/CC) using a chemical reduction method[33]. The introduction of Fe induced the redistribution of charges on the MoS_2 basal plane and generated new active sites, significantly improving the NH_3 synthesis performance. The NH_3 yield was 12.5 µg^{-1} h^{-1} cm^{-2} with FE of 10.8% at -0.1 V *vs.* Reversible Hydrogen Electrode (RHE). Moreover, the average size and chemical valence state of Fe nanodots did not change significantly after long-term electrolysis, which demonstrated the excellent stability of Fe-MoS_2/CC.
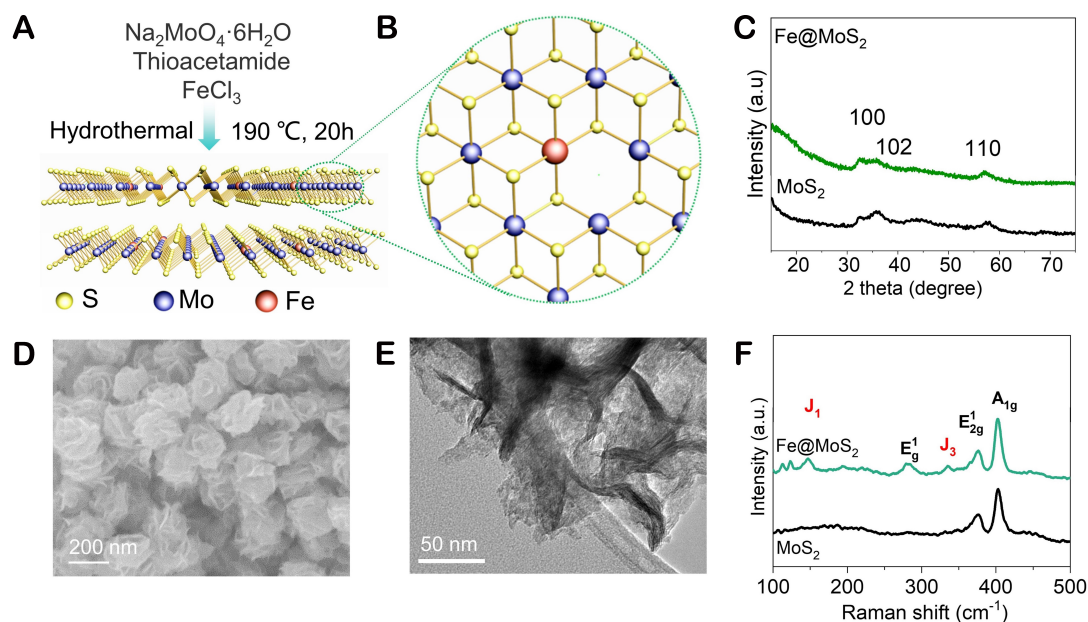
Figure 1. Schematic illustration of (A) synthesis process and (B) atomic structure; (C) XRD patterns of MoS_2 and Fe@MoS_2. (D) SEM image of Fe@MoS_2, (E) TEM image of Fe@MoS_2, (F) Raman spectra of MoS_2 and Fe@MoS_2.

In this work, we developed a synergetic optimization strategy to enhance the ENRR activity of MoS_2, coupling vacancy engineering, heteroatom doping, and phase engineering. Biomimetic Fe@MoS_2 electrocatalysts were prepared using a one-pot hydrothermal method. The partial MoS_2 converts from 2H to 1T phase after Fe atom doping. Furthermore, the unique hydrangea-like morphology and defects on the MoS_2 basal plane promote the accessibility of the active site. *In-situ* and electrochemical characterizations demonstrated that Fe atoms had been inserted into the lattice of MoS_2, and its unique coordination structure was analyzed which accelerates the reaction kinetics of N_2 to NH_3, thus achieving a promising ENRR performance. The maximum FE of 19.7% ± 5.5% and the highest NH_3 yield of 20.2 ± 5.3 μg h^{-1} mg^{-1} were achieved by Fe@MoS_2 at -0.2 V *vs.* RHE and -0.8 V *vs.* RHE, respectively.

MATERIALS AND METHODS

Synthesis of materials

One-step hydrothermal synthesis was used to prepare MoS_2 [Figure 1A]. Briefly, the mixed solution after sonication (30 mL deionized water (D.I water)) with 0.4 mmol $Na_2MoO_4 \cdot 6H_2O$ and 0.82 mmol thioacetamide) was transferred into a stainless steel autoclave (50 mL). The heating parameter was set to 190 °C for 20 h. After cooling, filtration, washing and drying at room temperature, MoS_2 was collected. The synthesis process of Fe@MoS_2 was the same as that of MoS_2, except for adding 0.004 mmol $FeCl_3$.

Electrochemical measurement

ENRR electrochemical performance was evaluated using a three-electrode system (0.25 M $LiClO_4$) under an ambient environment (25 °C, 1 atm). The working, reference, and counter electrodes are ENRR catalyst, Ag/AgCl (saturated KCl solution) electrode, and Pt wire, respectively. Firstly, 2 mg of catalyst was dispersed into 1 mL Nafion/ISO/D.I water solution (with the volume ratio of 1:9:40) with the sonication for 30 min. Then, 100 μL catalyst inks (MoS_2 and Fe@MoS_2) were drop-casted on carbon paper (1 cm²) with 0.2 mg cm^{-2} and dried in the ambient environment. Before the ENRR test, the electrolyte was bubbled with N_2 gas (purity, 99.99%) for 20 min. During the ENRR test, the N_2 flow was continuously inputted with a flow rate of 20 sccm.

Determination of NH₃

The quantification of NH_3 was determined using the salicylic acid-based colorimetric method[34]. To obtain the calibration curve, standard NH_4Cl solutions with different concentrations of 0.0, 0.1, 0.2, 0.5, 1.0, and 2.0 g mL⁻¹ in the electrolyte were first prepared. Then, 50 μL catalytic solution (10 mL D.I water with 0.1 g sodium nitroprusside dihydrate), 500 μL coloring solution (0.32 M NaOH and 0.4 M sodium salicylate), and 50 μL oxidation solution (NaClO solution (pCl = 4 - 4.9) with 0.75 M NaOH) were mixed with the 4 mL standard NH_4Cl solution, and standing for 1h for color development. Next, the ultraviolet-visible (UV-Vis) spectrophotometer was used to measure the absorbance (λ = 655 nm) with different concentrations of NH_4Cl. Finally, we got the calibration curve with a good linear relationship [Supplementary Figure 1]. The NH_3 concentration in the reaction electrolyte is calculated based on the standard curve.

The NH_3 formation rate can be calculated by:

$$R_{NH3}\left(\mu g \ h^{-1} \ mg^{-1} \right) = \frac{x(ppm) \times 10^3 \ (\mu g/mg) \times V(L)}{t(h) \times m(mg)}$$

where:

x (ppm): calculated concentration of ammonia.

V (L): volume of reacted electrolyte.

t (h): reaction time in hours.

m (mg): mass of catalyst on the carbon paper.

R_{NH3} μg h⁻¹ mg⁻¹

The FE is calculated using:

$$FE_{NH3}(\%) = \frac{3 \times R_{NH3}\left(\mu g \ h^{-1} \ mg^{-1} \right) \times t(h) \times 10^{-6} \ (g/\mu g) \times m(mg) \times F}{Mr_{NH4}(g/mol) \times I(A) \times t(s)} \times 100\%$$

where:

x (ppm): calculated concentration of ammonia.

Mr (NH_4^+): 18 (g/mol).

V (L): the volume of reacted electrolyte.

I (A): the average current during the reaction.

F: the Faraday constant 96,485 mol^{-1}.

Operando attenuated total reflection surface enhanced infrared absorption spectroscopy

Operando attenuated total reflection surface enhanced infrared absorption spectroscopy (ATR-SEIRAS) utilizes the same three-electrode system as the electrochemical test, and the electrolyte is 0.1 M Li$_2$SO$_4$ (N$_2$ saturated). Before each measurement, the background spectrum of the catalyst electrode needs to be collected at the open circuit potential. Afterward, the spectra at different potentials were collected. All collected spectra were given by the absorbance (-log(R/R_0)) with a spectral resolution of 4 cm^{-1}.

RESULTS AND DISCUSSION

Material characterization

The preparation process of Fe@MoS$_2$ and the atomic structure are illustrated in Figure 1A and 1B. X-ray diffraction (XRD) patterns of MoS$_2$ and Fe@MoS$_2$ are shown in Figure 1C. The diffraction peaks at 32.5°, 35.8°, and 57.2° could be indexed to (100), (102), and (110) planes of the standard MoS$_2$ phase (PDF #37-1492)[35-37], respectively. The diffraction peaks of Fe@MoS$_2$ do not change significantly compared to MoS$_2$, and no FeS or FeS$_2$ phases were observed, which indicates that traces of Fe element did not form new sulfide. A scanning electron microscopy (SEM) image [Figure 1D] shows that the synthesized Fe@MoS$_2$ is assembled from multiple 2D nanosheets and exhibits a hydrangea-like morphology. Moreover, Brunauer-Emmett-Teller (BET) test was carried out to characterize the specific surface area of catalysts. Supplementary Figure 2 shows the N$_2$ adsorption-desorption isotherm curve of MoS$_2$ and Fe@MoS$_2$. Fe@MoS$_2$ has a higher BET specific surface area of 54.034 m^2 g^{-1} and a higher pore volume of 0.32 cm^3 g^{-1} than MoS$_2$ (22.63 m^2 g^{-1} and 0.09 cm^3 g^{-1}, respectively). The catalytic activity was improved due to more exposed active sites [Supplementary Table 1]. The high specific surface area exposes more active sites, which benefits its catalytic activity. Electrochemically active surface area (ECSA) can be used to evaluate the number of active sites in a catalyst, which is proportional to the double-layer capacitance (C_{dl}). Supplementary Figure 3 presents the C_{dl} values obtained after linear fitting. Notably increased C_{dl} values were observed in Fe@MoS$_2$ (17.85 mF cm^{-2}), compared to MoS$_2$ (0.35 mF cm^{-2}), indicating the beneficial effect of Fe doping on the number of active sites.

No recognizable nanoparticles or clusters are observed in the transmission electron microscopy (TEM) image [Figure 1E]. This suggests that Fe was more likely to be inserted into the MoS$_2$ plane rather than deposited on the surface, which requires further analysis in combination with spectra. Raman spectra [Figure 1F] were employed to further investigate the effect of Fe insertion on MoS$_2$. The results suggest that synthesized MoS$_2$ exhibits distinct 2H phase signals, with two peak positions at 376.5 and 403 cm^{-1} corresponding to the E$^1_{2g}$ vibrational peak and A^1_g vibrational peak of 2H-MoS$_2$, respectively[35,38,39]. However, Fe@MoS$_2$ is a mixed 1T/2H-MoS$_2$ phase; two new 1T phase characteristic peaks of J$_1$ (146 cm^{-1}) and J$_3$ (334 cm^{-1}) are also clearly observed, indicating that the doping of Fe atoms triggers a phase transition from 2H-MoS$_2$ to 1T-MoS$_2$[40-42].

A high-resolution TEM (HRTEM) image [Figure 2A] shows the same results as those obtained from TEM images, with no impurities or other Fe-based structures observed in Fe@MoS$_2$. Further, with the help of dark field scanning TEM (STEM) characterization [Figure 2B and Supplementary Figure 4], it is seen that defects are present on the surface of the 2D structure. Atomic-level Fe (weak Z contrast intensity) replaces some Mo atoms and dopes in the panel of the 2D MoS$_2$ plane. To explore the distribution of different elements in the catalysts, corresponding energy dispersive spectroscopy (EDS) elemental mapping was
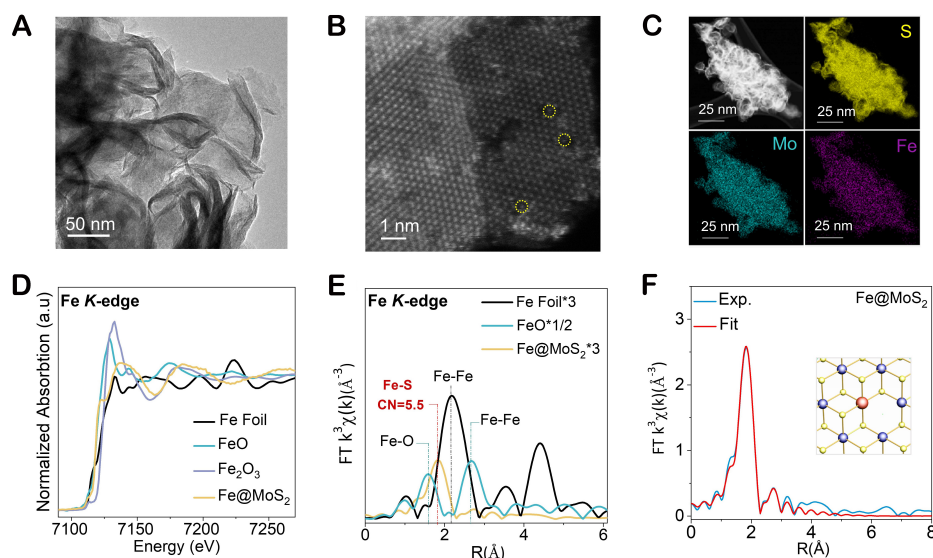
Figure 2. Material Characterization. (A) HRTEM image of Fe@MoS$_2$. (B) STEM image, and (C) the corresponding EDS elemental mappings of Fe@MoS$_2$, (D) XANES spectra of the Fe *K*-edge in Fe foil, FeO, Fe$_2$O$_3$, and Fe@MoS$_2$, (E) FT-EXAFS spectra of the Fe *K*-edge in Fe foil, FeO, and Fe@MoS$_2$. (F) XAFS fitting result of Fe@MoS$_2$ at *R* space. Inset: Atomic illustration of Fe@MoS$_2$ (Mo atoms: purple; S atoms: yellow; Fe atoms: red).

conducted to characterize Fe@MoS$_2$. Figure 2C demonstrates that Mo, S, and Fe are uniformly distributed in Fe@MoS$_2$.

X-ray absorption near edge structure (XANES) and Fourier transform-extended X-ray absorption fine structure (FT-EXAFS) spectra further revealed the coordination structure and coordination number of Fe atom in Fe@MoS$_2$. As shown in Figure 2D, the absorption edge of Fe@MoS$_2$ is close to the curve of FeO, indicating that Fe of Fe@MoS$_2$ is dominated by a chemical state of +2. In the FT-EXAFS spectra [Figure 2E], a peak can be observed at 1.87 Å for Fe@MoS$_2$, corresponding to the first coordination[43,44]. No Fe-O and Fe-Fe are observed in Fe@MoS$_2$, indicating that the atomically dispersed Fe may dope within Mo-based vacancy and bond with S atoms. Fitting curves [Figure 2F, Supplementary Figure 5, Supplementary Table 2] of the Fe *K*-edge EXAFS spectra of Fe@MoS$_2$ indicate that the Fe-S coordination number is approximately 5.5. This suggests that Fe primarily replaces the Mo atom and coordinates with five S atoms near the S vacancy in MoS$_2$.[45]. X-ray Photoelectron Spectroscopy (XPS) reveals the valence changes of the Mo and S elements after Fe doping. Figure 3A and B shows the S *2p* and Mo *3d* spectra of MoS$_2$ and Fe@MoS$_2$. Two characteristic peaks of 162.35 and 160.8 eV for MoS$_2$ were assigned to S *2p*$_{1/2}$ and S *2p*$_{3/2}$, respectively[46,47]. The introduction of Fe resulted in a positive shift of the peak position with altered binding energies of 162.70 and 161.20 eV, which may be related to the Fe-S bond formation. In addition, the peaks with binding energies at 230.9 and 227.7 eV correspond to Mo *3d*$_{3/2}$ and Mo *3d*$_{5/2}$[48]. A positive shift of 1.1 eV was observed in Fe@MoS$_2$, indicating an elevated valence state for Mo as well, which is well in line with the previously reported research[49,50].

Electrochemical measurements

The ENRR performance of the Fe@MoS$_2$ is evaluated in an H-type cell equipped with a three-electrode system [Figure 4A]. The linear scan voltammetry (LSV) was first performed to compare the response current density under Ar- or N$_2$-saturated electrolyte of Fe@MoS$_2$. As shown in Figure 4B, higher current density in N$_2$ indicates the possibility of the Fe@MoS$_2$ towards N$_2$ reduction. The subsequent ENRR
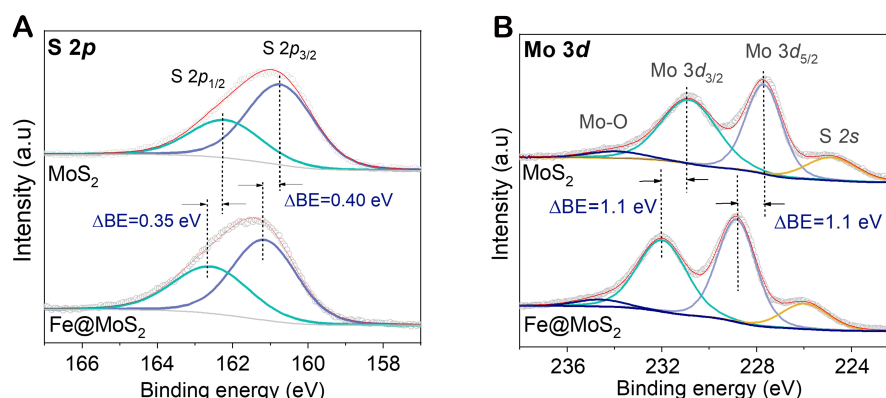
Figure 3. (A) S 2*p* and (B) Mo 3*d* XPS of MoS_2 and Fe@MoS_2.
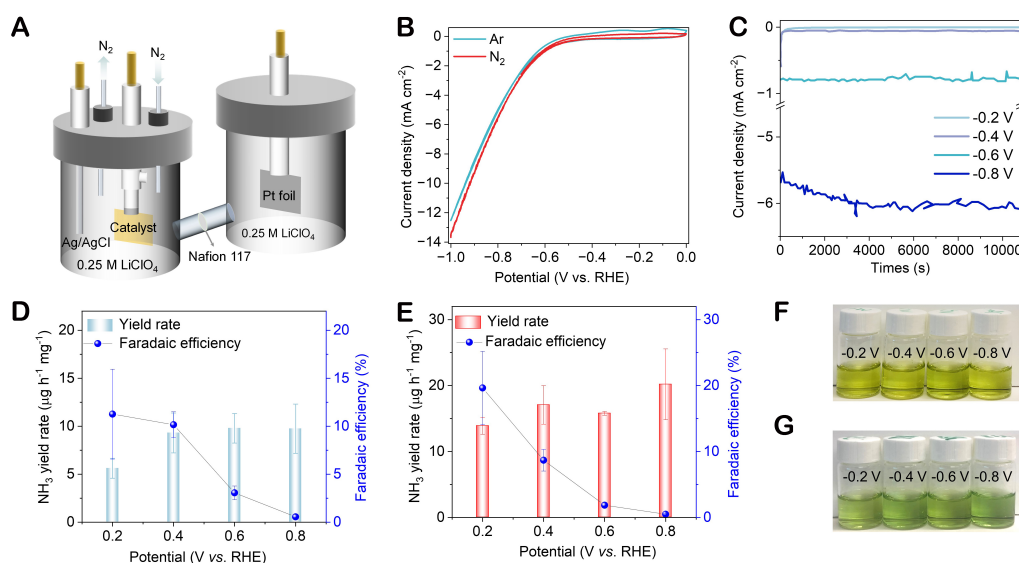
Figure 4. Electrochemical performance evaluation. (A) Schematic illustration of the reactor for electrochemical N_2 reduction. (B) LSV curves of Fe@MoS_2 in Ar and N_2-saturated 0.25 M $LiClO_4$ at a scan rate of 10 mV s^{-1}. (C) Chronoamperometric curves of Fe@MoS_2 at different applied potentials. NH_3 yield rate and FE of (D) MoS_2 and (E) Fe@MoS_2. The picture of the reacted solution of (F) MoS_2 and (G) Fe@MoS_2.

performance was evaluated using a chronoamperometry method in N_2-saturated electrolyte for 3 h, and the response current densities at different potentials were recorded [Figure 4]. The reacted electrolyte was collected and analyzed for the NH_3 concentration[34]. The relevant equations have been mentioned above.

The yield rate and FE of NH_3 over the electrocatalyst Fe@MoS_2 are higher than those of the pristine MoS_2 electrocatalyst, which indicates the optimization of the introduction of Fe element in the pristine MoS_2 plane. As shown in Figure 4D, the MoS_2 can achieve the yield rate of NH_3 less than 10 μg h^{-1} mg^{-1} between the potential of -0.2 to -0.8 V *vs.* RHE, while the Fe@MoS_2 can achieve the yield rate of NH_3 larger than 13.9 μg h^{-1} mg^{-1}. The highest yield rate of 20.2 ± 5.3 μg h^{-1} mg^{-1} is obtained at -0.8 V *vs.* RHE, about two times higher than that of MoS_2 [Figure 4E]. As shown in Figure 4F and G, the colors of the reacted electrolytes of Fe@MoS_2 and MoS_2 are green and yellow, respectively, suggesting that more NH_3 is generated with Fe@MoS_2 than that of MoS_2. The highest FE of ~19.7% ± 5.5% is obtained at -0.2 V *vs.* RHE. The FE
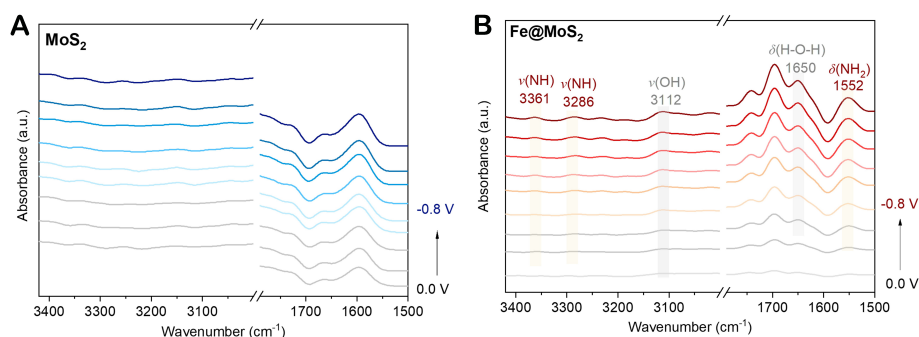
Figure 5. Mechanism study. Operando ATR-SEIRAS of (A) MoS_2 and (B) Fe@MoS_2.

dramatically decreases as the applied potentials increase, suggesting that the reaction is dominated by side-reaction HER. Compared with previously reported MoS_2-based catalysts, Supplementary Table 3 shows that Fe@MoS_2 exhibits a relatively high FE and yield rate of NH_3. In addition, Fe@MoS_2 demonstrates reliable stability in long-term (10 h) stability tests. Supplementary Figure 6 illustrates no significant deterioration of the current density of Fe@MoS_2.

Operando ATR-SEIRAS was performed to characterize the reaction intermediates and study the reaction mechanism. Figure 5 recorded the ATR-SEIRAS spectra of MoS_2 and Fe@MoS_2 under different potentials during the ENRR process. As shown in Figure 5A, no obvious peak can be observed for pristine MoS_2, indicating no intermediates generated. In contrast, several peaks gradually increase with the increasing potentials for Fe@MoS_2 [Figure 5B]. Some peaks attributed to N-H stretching are located at 3,361 and 3,286 cm^{-1}[51,52]. The peaks at 3,112 and 1,650 cm^{-1} correspond to the O-H stretching and bending mode of H_2O, respectively[53,54]. The bending vibration absorption peak of -N-H at 1,552 cm^{-1} gradually strengthened[55], indicating a strong N_2 reduction reaction over the Fe@MoS_2. These results demonstrate that introducing Fe can accelerate the ENRR kinetics.

CONCLUSIONS

In conclusion, an inspired biomimetic electrocatalyst of Fe@MoS_2 is designed and successfully prepared using a one-step hydrothermal method. The introduction of atomic-level Fe achieves the geometric and electronic structure modulation of MoS_2 and triggers the phase transition of the 2H-phase MoS_2 into 1T-phase MoS_2. Thanks to the improved atomic structure and increased electrical conductivity of Fe@MoS_2, the kinetics are greatly accelerated, thus enhancing ENRR performance. Compared to the pristine 2H MoS_2, the prepared Fe@MoS_2 boosts the ENRR kinetics and exhibits superior ENRR performance with a yield rate of 20.2 ± 5.3 μg h^{-1} mg^{-1} at -0.8 V *vs*. RHE and a FE of ~19.7% ± 5.5% at -0.2 V *vs*. RHE. This work provides a new insight for designing efficient ENRR catalysts by synergistic doping and phase engineering.

DECLARATIONS

Authors' contributions
Synthesis and testing of materials, data collection, and original manuscript writing: Jia Y, Shao G, Li Y, Yang R
Validation and original manuscript revision: Huang M, Huang H, Liu M, Huang G, Lu Q, Gu C
Data collection: Jia Y, Shao G, Li Y, Yang R
Data analysis, writing, review, and editing: Jia Y, Li Y, Shao G

Review and discussion: Jia Y, Li Y, Shao G, Huang H, Huang G, Gu C
Supervision, funding acquisition: Li Y, Huang M
All authors have read and agreed to the published version of the manuscript.

Availability of data and materials
According to reasonable requirements, all of the data examined in this research can be obtained from the correspondents.

Financial support and sponsorship

Conflicts of interest
Liu M is affiliated with "State Grid Zhejiang Electric Power CO., LTD Research Institute, Hangzhou, China". While the other authors have declared that they have no conflicts of interest.

Ethical approval and consent to participate
Not applicable.

Consent for publication
Not applicable.

Copyright

REFERENCES

1. Wang J, Yu L, Hu L, Chen G, Xin H, Feng X. Ambient ammonia synthesis via palladium-catalyzed electrohydrogenation of dinitrogen at low overpotential. *Nat Commun* 2018;9:1795. DOI PubMed PMC
2. Suryanto BHR, Matuszek K, Choi J, et al. Nitrogen reduction to ammonia at high efficiency and rates based on a phosphonium proton shuttle. *Science* 2021;372:1187-91. DOI
3. Guo J, Chen P. Catalyst: NH_3 as an energy carrier. *Chem* 2017;3:709-12. DOI
4. Chang F, Gao W, Guo J, Chen P. Emerging materials and methods toward ammonia-based energy storage and conversion. *Adv Mater* 2021;33:e2005721. DOI PubMed
5. Cechetto V, Di Felice L, Gallucci F. Advances and perspectives of H_2 production from NH_3 decomposition in membrane reactors. *Energy Fuels* 2023;37:10775-98. DOI PubMed PMC
6. He W, Zhang J, Dieckhöfer S, et al. Splicing the active phases of copper/cobalt-based catalysts achieves high-rate tandem electroreduction of nitrate to ammonia. *Nat Commun* 2022;13:1129. DOI PubMed PMC
7. Wang L, Xia M, Wang H, et al. Greening ammonia toward the solar ammonia refinery. *Joule* 2018;2:1055-74. DOI
8. Weng G, Lei S, Wang R, et al. A high-efficiency electrochemical proton-conducting membrane reactor for ammonia production at intermediate temperatures. *Joule* 2023;7:1333-46. DOI
9. Chen G, Yuan Y, Jiang H, et al. Electrochemical reduction of nitrate to ammonia via direct eight-electron transfer using a copper - molecular solid catalyst. *Nat Energy* 2020;5:605-13. DOI
10. Sun J, Alam D, Daiyan R, et al. A hybrid plasma electrocatalytic process for sustainable ammonia production. *Energy Environ Sci* 2021;14:865-72. DOI
11. Arif M, Babar M, Azhar U, et al. Rational design and modulation strategies of Mo-based electrocatalysts and photo/electrocatalysts towards nitrogen reduction to ammonia (NH_3). *Chem Eng J* 2023;451:138320. DOI
12. Mukherjee S, Yang X, Shan W, et al. Atomically dispersed single Ni site catalysts for nitrogen reduction toward electrochemical ammonia synthesis using N_2 and H_2O. *Small Methods* 2020;4:1900821. DOI
13. Zheng J, Jiang L, Lyu Y, Jiang SP, Wang S. Green synthesis of nitrogen-to-ammonia fixation: past, present, and future. *Energy Environ Mater* 2022;5:452-7. DOI
14. Danyal K, Dean DR, Hoffman BM, Seefeldt LC. Electron transfer within nitrogenase: evidence for a deficit-spending mechanism.

Biochemistry 2011;50:9255-63. DOI PubMed PMC

15.   Foster SL, Bakovic SIP, Duda RD, et al. Catalysts for nitrogen reduction to ammonia. *Nat Catal* 2018;1:490-500. DOI

16.   Shi Z, Zhang X, Lin X, et al. Phase-dependent growth of Pt on MoS$_2$ for highly efficient H$_2$ evolution. *Nature* 2023;621:300-5. DOI

17.   Chen S, Liu X, Xiong J, Mi L, Li Y. Engineering strategies for boosting the nitrogen reduction reaction performance of MoS$_2$-based electrocatalysts. *Materials Today Nano* 2022;18:100202. DOI

18.   Li Y, Gu Q, Johannessen B, et al. Synergistic Pt doping and phase conversion engineering in two-dimensional MoS$_2$ for efficient hydrogen evolution. *Nano Energy* 2021;84:105898. DOI

19.   Li Y, Wang H, Xie L, Liang Y, Hong G, Dai H. MoS$_2$ nanoparticles grown on graphene: an advanced catalyst for the hydrogen evolution reaction. *J Am Chem Soc* 2011;133:7296-9. DOI

20.   Zhang L, Ji X, Ren X, et al. Electrochemical ammonia synthesis via nitrogen reduction reaction on a MoS$_2$ catalyst: theoretical and experimental studies. *Adv Mater* 2018;30:e1800191. DOI

21.   Li J, Wei F, Dong C, Wang Z, Xiu Z, Han X. Recent progress of inorganic metal-based catalysts in electrocatalytic synthesis of ammonia. *Mater Today Energy* 2021;21:100766. DOI

22.   Karunadasa HI, Montalvo E, Sun Y, Majda M, Long JR, Chang CJ. A molecular MoS$_2$ edge site mimic for catalytic hydrogen generation. *Science* 2012;335:698-702. DOI PubMed

23.   Yan Z, Ji M, Xia J, Zhu H. Recent advanced materials for electrochemical and photoelectrochemical synthesis of ammonia from dinitrogen: one step closer to a sustainable energy future. *Adv Energy Mater* 2020;10:1902020. DOI

24.   Ren Y, Yu C, Tan X, Huang H, Wei Q, Qiu J. Strategies to suppress hydrogen evolution for highly selective electrocatalytic nitrogen reduction: challenges and perspectives. *Energy Environ Sci* 2021;14:1176-93. DOI

25.   Wu W, Wang L, Li Y, et al. Piezoelectricity of single-atomic-layer MoS$_2$ for energy conversion and piezotronics. *Nature* 2014;514:470-4. DOI

26.   Fei H, Guo T, Xin Y, et al. Sulfur vacancy engineering of MoS$_2$ via phosphorus incorporation for improved electrocatalytic N$_2$ reduction to NH$_3$. *Appl Catal B Environ* 2022;300:120733. DOI

27.   Fei H, Liu R, Wang J, et al. Targeted modulation of competitive active sites toward nitrogen fixation via sulfur vacancy engineering over MoS$_2$. *Adv Funct Mater* 2023;33:2302501. DOI

28.   Niu L, Wang D, Xu K, et al. Tuning the performance of nitrogen reduction reaction by balancing the reactivity of N$_2$ and the desorption of NH$_3$. *Nano Res* 2021;14:4093-9. DOI

29.   Guo J, Tadesse Tsega T, Ul Islam I, Iqbal A, Zai J, Qian X. Fe doping promoted electrocatalytic N$_2$ reduction reaction of 2H MoS$_2$. *Chin Chem Lett* 2020;31:2487-90. DOI

30.   Lin G, Ju Q, Guo X, et al. Intrinsic electron localization of metastable MoS$_2$ boosts electrocatalytic nitrogen reduction to ammonia. *Adv Mater* 2021;33:e2007509. DOI

31.   Wu Z, Zhang R, Fei H, Liu R, Wang D, Liu X. Multiphasic 1T@2H MoSe$_2$ as a highly efficient catalyst for the N$_2$ reduction to NH$_3$. *Appl Surface Sci* 2020;532:147372. DOI

32.   You M, Yi S, Hou X, et al. High temperature induced S vacancies in natural molybdenite for robust electrocatalytic nitrogen reduction. *J Colloid Interface Sci* 2021;599:849-56. DOI

33.   Zhao X, Zhang X, Xue Z, Chen W, Zhou Z, Mu T. Fe nanodot-decorated MoS$_2$ nanosheets on carbon cloth: an efficient and flexible electrode for ambient ammonia synthesis. *J Mater Chem A* 2019;7:27417-22. DOI

34.   Ivancic I, Degobbis D. An optimal manual procedure for ammonia analysis in natural waters by the indophenol blue method. *Water Res* 1984;18:1143-7. DOI

35.   Kamila S, Mohanty B, Samantara AK, et al. Highly active 2D layered MoS$_2$-rGO hybrids for energy conversion and storage applications. *Sci Rep* 2017;7:8378. DOI PubMed PMC

36.   Sun T, Li Z, Liu X, Ma L, Wang J, Yang S. Facile construction of 3D graphene/MoS$_2$ composites as advanced electrode materials for supercapacitors. *J Power Sources* 2016;331:180-8. DOI

37.   Liu Y, Chen Y, Tian Y, et al. Synergizing hydrogen spillover and deprotonation by the internal polarization field in a MoS$_2$/NiPS$_3$ vertical heterostructure for boosted water electrolysis. *Adv Mater* 2022;34:e2203615. DOI

38.   Wang R, Xu C, Sun J, et al. Heat-induced formation of porous and free-standing MoS$_2$/GS hybrid electrodes for binder-free and ultralong-life lithium ion batteries. *Nano Energy* 2014;8:183-95. DOI

39.   Qian X, Zhu G, Wang K, et al. Bowl-like mesoporous polymer-induced interface growth of molybdenum disulfide for stable lithium storage. *Chem Eng J* 2020;381:122651. DOI

40.   Zhao Y, Chang K, Gu Q, et al. Noble metal-free 2D 1T-MoS$_2$ edge sites boosting selective hydrogenation of maleic anhydride. *ACS Catal* 2022;12:8986-94. DOI

41.   Sheng Z, Qi P, Lu Y, et al. Nitrogen-doped metallic MoS$_2$ derived from a metal-organic framework for aqueous rechargeable zinc-ion batteries. *ACS Appl Mater Interfaces* 2021;13:34495-506. DOI

42.   Hu X, Zeng X, Liu Y, et al. Nano-layer based 1T-rich MoS$_2$/g-C$_3$N$_4$ co-catalyst system for enhanced photocatalytic and photoelectrochemical activity. *Appl Catal B Environ* 2020;268:118466. DOI

43.   Li J, Zhang Y, Liu C, et al. 3.4% Solar-to-ammonia efficiency from nitrate using Fe single atomic catalyst supported on MoS$_2$ nanosheets. *Adv Funct Mater* 2022;32:2108316. DOI

44.   Cao Y, Zhang Y, Yang L, et al. Boosting oxygen reduction reaction kinetics through perturbating electronic structure of single-atom Fe-N$_3$S$_1$ catalyst with sub-nano FeS cluster. *J Colloid Interface Sci* 2023;650:924-33. DOI

45. Chen K, Wang J, Kang J, Lu X, Zhao X, Chu K. Atomically Fe-doped MoS_{2-x} with Fe-Mo dual sites for efficient electrocatalytic NO reduction to NH_3. *Appl Catal B Environ* 2023;324:122241. DOI

46. Zhao W, Yuan S, Lei S, et al. Tailoring rational crystal orientation and tunable sulfur vacancy on metal-sulfides toward advanced ultrafast ion-storage capability. *Adv Funct Mater* 2023;33:2211542. DOI

47. Baker M, Gilmore R, Lenardi C, Gissler W. XPS investigation of preferential sputtering of S from MoS_2 and determination of MoS_x stoichiometry from Mo and S peak positions. *Appl Surface Sci* 1999;150:255-62. DOI

48. Wang F, Zhang W, Jiang J, et al. Nitrogen-rich carbon-supported ultrafine MoC nanoparticles for the hydrotreatment of oleic acid into diesel-like hydrocarbons. *Chem Eng J* 2020;382:122464. DOI

49. Xue JY, Li FL, Zhao ZY, et al. In Situ generation of bifunctional Fe-doped MoS_2 nanocanopies for efficient electrocatalytic water splitting. *Inorg Chem* 2019;58:11202-9. DOI

50. Li H, Cheng M, Wang P, et al. Reducing contact resistance and boosting device performance of monolayer MoS_2 by in situ Fe doping. *Adv Mater* 2022;34:e2200885. DOI

51. Liu S, Meng X, Xu J, Zhou H, Liu S, Wang J. Porous Si@C composite anode material prepared using dopamine as a carbon source for high-performance lithium- ion batteries. *Int J Electrochem Sci* 2020;15:3479-94. DOI

52. Zou W, Yeo SY. Characterization of freeze-thaw treatments upon binders in ancient chinese wall paintings by X-ray diffraction (XRD) and attenuated total reflection - fourier transform infrared (ATR-FTIR) spectroscopy. *Anal Lett* 2024;57:190-201. DOI

53. Rozenberg M, Jung C, Shoham G. Low temperature FTIR spectra and hydrogen bonds in polycrystalline cytidine. *Spectrochim Acta A* 2004;60:2369-75. DOI

54. Liu S, Qian T, Wang M, et al. Proton-filtering covalent organic frameworks with superior nitrogen penetration flux promote ambient ammonia synthesis. *Nat Catal* 2021;4:322-31. DOI

55. Wang B, Jiang Y, Zhao F. Synthesis of mussel-inspired silica nanocomposites for efficient removal of methyl orange. *Mater Lett* 2022;314:131832. DOI